

This is the accepted manuscript made available via CHORUS. The article has been published as:

## Controlling dispersive hydrodynamic wavebreaking in a viscous fluid conduit

Dalton V. Anderson, Michelle D. Maiden, and Mark A. Hoefer

Phys. Rev. Fluids **4**, 074804 — Published 17 July 2019

DOI: [10.1103/PhysRevFluids.4.074804](https://doi.org/10.1103/PhysRevFluids.4.074804)

# Controlling Dispersive Hydrodynamic Wavebreaking in a Viscous Fluid Conduit

Dalton V. Anderson,<sup>\*</sup> Michelle D. Maiden,<sup>†</sup> and Mark A. Hoefer<sup>‡</sup>

*Department of Applied Mathematics, University of Colorado, Boulder, Colorado 80302, USA*

(Dated: May 15, 2019)

The driven, cylindrical, free interface between two miscible, Stokes fluids with high viscosity contrast have been shown to exhibit dispersive hydrodynamics. A hallmark feature of dispersive hydrodynamic media is the dispersive resolution of wavebreaking that results in a dispersive shock wave. In the context of the viscous fluid conduit system, the present work introduces a simple, practical method to precisely control the location, time, and spatial profile of wavebreaking in dispersive hydrodynamic systems with only boundary control. The method is based on tracking the dispersionless characteristics backward from the desired wavebreaking profile to the boundary. In addition to the generation of approximately step-like Riemann and box problems, the method is generalized to other, approximately piecewise-linear dispersive hydrodynamic profiles including the triangle wave and N-wave. A definition of dispersive hydrodynamic wavebreaking is used to obtain quantitative agreement between the predicted location and time of wavebreaking, viscous fluid conduit experiment, and direct numerical simulations for a range of flow conditions. Observed space-time characteristics also agree with triangle and N-wave predictions. The characteristic boundary control method introduced here enables the experimental investigation of a variety of wavebreaking profiles and is expected to be useful in other dispersive hydrodynamic media. As an application of this approach, soliton fission from a large, box-like disturbance is observed both experimentally and numerically, motivating future analytical treatment.

Keywords: Dispersive shock waves

## I. INTRODUCTION

The interfacial dynamics of a viscous fluid conduit exhibit a wide range of dispersive hydrodynamic behavior observable in other geophysical, superfluidic, optical, and condensed matter media [1]. A viscous fluid rises buoyantly through a more viscous, stationary fluid and, under appropriate conditions, the interface resembles that of a deformable pipe. The interface's dynamics can be accurately described by the conduit equation [2–4], a nonlinear dispersive partial differential equation that has been shown to admit a rich zoology of multiscale coherent wave solutions [5]. Experimentally, solitons [2, 6, 7], dispersive shock waves (DSWs), and the interactions between them [8–10] have been observed to be in excellent agreement with conduit equation predictions. In this sense, the viscous fluid conduit is an ideal laboratory environment for the study of dispersive hydrodynamics.

Dispersive shock waves are coherent structures that are fundamental to dispersive hydrodynamics [1]. The first applications of conservative, dispersive hydrodynamic models to hydrodynamic wavebreaking occurred in the context of undular bores in water waves [11] and collisionless shocks in plasma [12]. A common feature in both these and subsequent dispersive hydrodynamic applications, is the fundamentally unique nature of wavebreaking. Conservative wave dispersion compensates nonlinear

self-steepening to give rise to an expanding, oscillatory train of amplitude-ordered nonlinear waves bookended by a large amplitude solitary wave and a packet of small amplitude dispersive waves. To distinguish conservative, dispersive wavebreaking from its counterpart in dissipative media that gives rise to steady, viscous shock waves [13], the term dispersive shock wave or DSW has been adopted [1]. As in classical gas dynamics [14], the model problem for shock generation is the Riemann problem that consists of an initial, sharp step in amplitude.

A major challenge for the experimental study of DSWs is the controlled realization of wavebreaking that involves the spontaneous generation of oscillations when nonlinear self-steepening enhances small-scale dispersive processes. One obstacle to the laboratory generation of a desired wavebreaking profile is its reliable initiation from only boundary control. Laboratory nonlinear dispersive wave environments constrained by boundary control include fluids such as shallow water wave tanks (see, e.g. [15]) and viscous fluid conduits [6]. Also included are non-fluid systems such as intense laser light propagation in optical fibers [16], magnetic spin waves [17], and granular crystals [18]. It can be difficult to achieve controlled wavebreaking conditions without boundary interactions. Here, we report on a simple mathematical observation that yields a feasible way to achieve a variety of wavebreaking profiles away from boundaries. We track the (long-wave) characteristics of the dispersionless conduit equation backwards in time from the desired wavebreaking profile. The resulting solution is then used as a boundary condition for conduit experiments to realize a variety of wavebreaking profiles at desired spatial locations. This technique was used to generate dispersive hydrodynamic flows in a viscous fluid conduit [9, 10].

---

<sup>\*</sup> Also at Department of Aerospace Engineering, University of Colorado, Boulder, CO 80302, USA.

<sup>†</sup> Michelle.Maiden@Colorado.edu

<sup>‡</sup> <https://www.colorado.edu/amath/research/dispersive-hydrodynamics-lab>

In a related work in laser propagation through a nonlinear fiber [19], experimentalists created hyperbolic simple waves aided by the corresponding dispersionless long-wave shallow water model.

Changing between boundary and initial conditions is a useful tool in the study of nonlinear waves. The piston shock problem is a canonical boundary value problem in the theory of classical shock waves. G. B. Whitham reformulated the problem by tracing characteristics back from the piston to an equivalent initial value problem that was then solved via the method of characteristics [20]. Here, we do the reverse by converting a desired initial value problem into a boundary value problem in the context of dispersive shock waves. We use this approach to precisely realize several wavebreaking profiles in experiment: step, box, triangle, and N-wave configurations. We find that, despite neglecting short-wave dispersion, we can precisely control the location and time of wavebreaking as well as the long-wave characteristics that lead up to breaking. This is supported both theoretically by numerical simulations of the conduit equation and experimentally with our viscous conduit setup. This control method is also used to generate a large number of solitary waves (soliton fission) from a box profile. This relatively simple approach turns out to be quite effective and could be applied to other dispersive hydrodynamic media. Indeed, dispersive hydrodynamic wavebreaking and its control have played a decisive role in recent shallow water experiments [15, 21] and intense light propagation in defocusing, optical media [19, 22].

The paper is organized as follows. Section II is the theoretical section and includes background information on the conduit equation and the mathematical procedure for converting the initial value problem into a boundary value problem. Section III is the experimental section and covers both numerical and experimental methods and analysis. Conclusions are in Section IV.

## II. THEORY

### A. Conduit Equation

Conduits generated by the low Reynolds number, buoyant dynamics of two miscible fluids with differing densities and viscosities were first studied in the context of geological and geophysical processes [23]. We create viscous fluid conduits with glycerine as the exterior fluid and dyed, diluted glycerine as the interior fluid. Long-wave, slowly varying perturbations to a uniform background conduit result in the conduit equation [2, 3]

$$A_T + \frac{g\Delta}{8\pi\mu^{(i)}} (A^2)_Z - \frac{\mu^{(e)}}{8\pi\mu^{(i)}} (A^2 (A^{-1}A_T)_Z)_Z = 0, \quad (1)$$

where  $\mu^{(i)}$  is the interior dynamic viscosity,  $\mu^{(e)}$  is the exterior dynamic viscosity,  $\Delta = \rho^{(e)} - \rho^{(i)}$  is the difference in exterior to interior fluid densities, and  $g$  is

gravitational acceleration. This equation approximately governs the evolution of the circular interface with cross-sectional area  $A$  at vertical height  $Z$  and time  $T$ . The simplest wavebreaking configuration is a step decrease in conduit area

$$A(Z, T_b) = \begin{cases} A_2, & Z < Z_b \\ A_1, & Z \geq Z_b \end{cases}, \quad (2)$$

for some  $A_2 > A_1 = \pi R_0^2$ , where  $R_0$  is the conduit radius,  $Z_b$  is the breaking location, and  $T_b$  is the breaking time. We can nondimensionalize the equation and rescale the leading area to unity via the scalings

$$a = \frac{1}{\pi R_0^2} A, \quad z = \frac{\sqrt{8\varepsilon}}{R_0} Z, \quad t = \frac{gR_0\Delta\sqrt{\varepsilon}}{\sqrt{8\mu^{(i)}}} T, \quad (3)$$

where  $\varepsilon = \frac{\mu^{(i)}}{\mu^{(e)}}$  is the interior to exterior viscosity ratio. Then, the conduit equation in nondimensional form is

$$a_t + (a^2)_z - (a^2(a^{-1}a_t)_z)_z = 0, \quad z \in \mathbb{R}, \quad t > t_b. \quad (4)$$

We represent the desired wavebreaking profile via the data  $a(z, t_b) = a_0(z)$ . For example the step profile (2) is

$$a_0(z) = \begin{cases} a_b, & z < z_b \\ 1, & z \geq z_b \end{cases}, \quad z \in \mathbb{R}. \quad (5)$$

where  $a_b = A_2/A_1 > 1$  is the jump ratio and  $z_b, t_b$  are the nondimensional breaking height and time, respectively. We also consider the box profile of amplitude  $a_b$  and width  $w$ ,

$$a_0(z) = \begin{cases} a_b, & z_b - w < z < z_b \\ 1, & \text{else} \end{cases}, \quad z \in \mathbb{R}, \quad (6)$$

the triangle profile of amplitude  $a_b$ , width  $w$ , and hypotenuse slope  $m = \frac{a_b-1}{w}$ ,

$$a_0(z) = \begin{cases} mz + (a_b - mz_b), & z_b - w < z < z_b \\ 1, & \text{else} \end{cases}, \quad z \in \mathbb{R}, \quad (7)$$

and the N-wave profile of maximum amplitude  $a_{max}$ , minimum amplitude  $a_{min}$ , width  $w$ , and slope  $m = \frac{a_{max}-a_{min}}{w}$ ,

$$a_0(z) = \begin{cases} mz + (a_b - mz_b), & z_b - w < z < z_b \\ 1, & \text{else} \end{cases}, \quad z \in \mathbb{R}. \quad (8)$$

For example profiles, see Fig. 1.

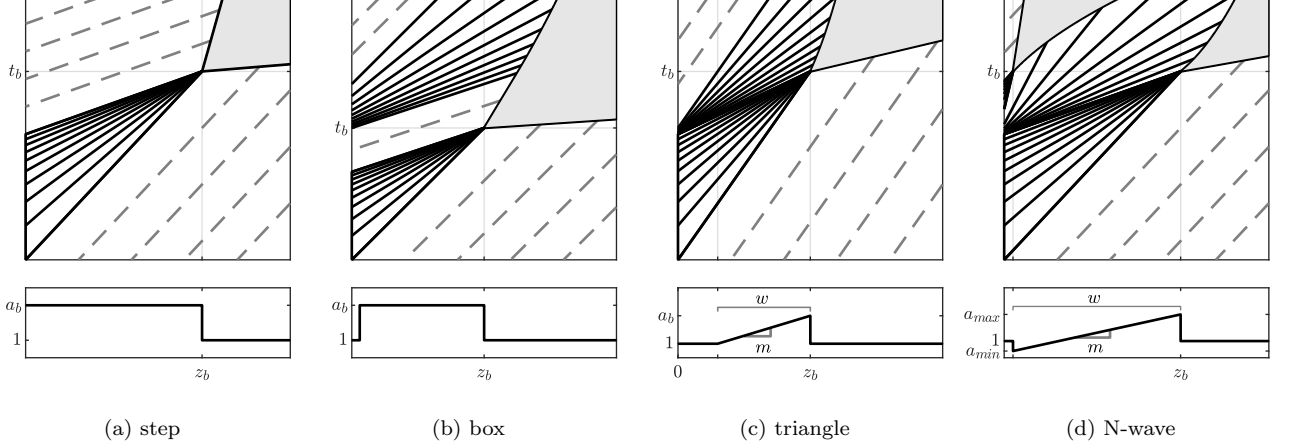


FIG. 1. Characteristic plots (large plots) and wavebreaking profiles at time of breaking (small plots). The gray regions are areas where wavebreaking has occurred and small-scale dispersion is important so the inviscid Burger's solution is no longer valid. The light vertical and horizontal lines depict strong and weak discontinuities in the profiles at the time of breaking. Shown here are step (a), box (b), triangle (c), and N-wave (d) wavebreaking profiles.

## B. Inviscid Burgers Equation

In order to approximately realize the breaking configurations that give rise to  $a_0(z)$ , e.g. (5)–(8), we seek to identify the spatio-temporal profile for times *prior* to breaking  $t < t_b$ . We assume that prior to DSW formation, the third order dispersive term is negligible. A dimensional analysis of eq. (1) shows that the nonlinear advective term dominates the dispersive term prior to breaking if

$$Z_b \gg \frac{\mu^{(e)}}{g\Delta T_b}, \quad (9)$$

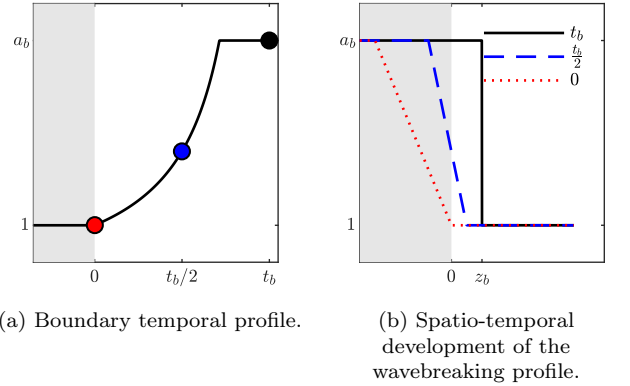
where  $Z_b$  and  $T_b$  are the dimensional breaking height and time, respectively. For the experiments reported here,  $\mu^{(e)}/(g\Delta) \approx 0.30 \text{ s cm}$ ,  $T_b \in (80, 140) \text{ s}$ , and  $Z_b \in (15, 27) \text{ cm}$ . Therefore, we are well within the expected regime of validity. We will further justify the assumption of dispersionless dynamics with numerical and physical experiments. This is a long-wave assumption that is valid when  $|a_z|/|a| \sim |a_t|/|a| \ll 1$ , when nonlinearity exceeds wave dispersion. We therefore neglect the dispersive term,  $(a^2(a^{-1}a_t)_z)_z$  in (4), and reverse time and shift space via

$$z = \zeta + z_b, \quad t = -(\tau - t_b), \quad a = u, \quad (10)$$

where  $u(\zeta, \tau)$  now satisfies the time-reversed inviscid Burgers Equation,

$$u_\tau - (u^2)_\zeta = 0, \quad \tau > 0, \quad \zeta \in \mathbb{R} \quad (11)$$

$$u(\zeta, 0) = u_0(\zeta) = a_0(\zeta - z_b), \quad (12)$$



(a) Boundary temporal profile.

(b) Spatio-temporal development of the wavebreaking profile.

FIG. 2. (a) Temporal profile of the boundary condition Eq. (17). (b) Evolution of the rescaled rarefaction wave Eq. (17). As time moves forward, the wave approaches the desired step. The dots in (a) correspond to the times depicted in (b), from left to right.

which has the implicit solution

$$u(\zeta, \tau) = u_0(\zeta + 2u(\zeta, \tau)\tau). \quad (13)$$

Then, converting (13) back to conduit equation variables and evaluating at the boundary  $z = 0$ , we have an implicit form of the boundary condition in terms of the known initial condition  $a_0(z)$ ,

$$a(0, t) = a_0(-2a(0, t)t). \quad (14)$$

A necessary condition that precludes breaking for  $0 < t < t_b$  is  $a'_0(z) < 1/2t_b$  for all  $z$ .

We now consider the specific case of step data (5).

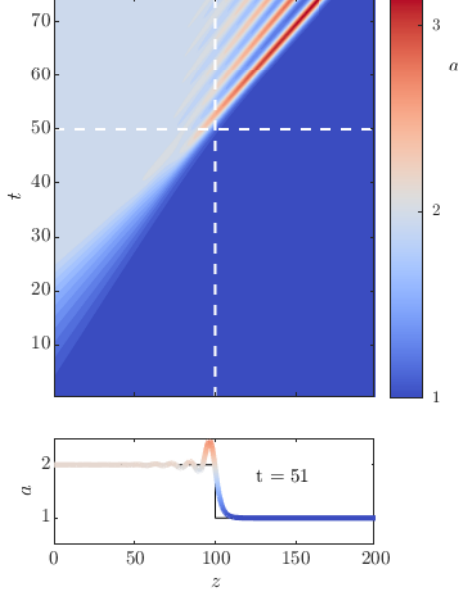


FIG. 3. Numerical simulation of the conduit equation with initial condition  $a(z, 0) = 1$  and the boundary condition equation (17) with  $z_b = 100$  and  $a_b = 2$ . The predicted  $z_b = 100$  and  $t_b = 50$  are identified by the intersection of the vertical and horizontal dashed lines. The oscillatory wave profile at the extracted time and location of breaking  $t_b = 51$ ,  $z_b = 97$  (see Sec. IIC) and its corresponding theoretical step profile are shown in the lower panel.

For this case, the self-similar, rarefaction wave solution is operable

$$u(\zeta, \tau) = \begin{cases} u_- & : \zeta \leq 2u_- \tau, \\ \frac{\zeta}{2\tau} & : 2u_- \tau \leq \zeta \leq 2u_+ \tau, \\ u_+ & : \zeta \geq 2u_+ \tau. \end{cases} \quad (15)$$

The substitution (10) along with

$$t_b = \frac{z_b}{2} \frac{a_b - 1}{a_b}, \quad u_- = 1, \quad u_+ = a_b \quad (16)$$

yields the sought for boundary condition

$$a(0, t) = \begin{cases} 1 & : t \leq 0 \\ (1 - 2t/z_b)^{-1} & : 0 < t < \frac{(a_b - 1)}{2a_b} z_b \\ a_b & : t \geq \frac{(a_b - 1)}{2a_b} z_b \end{cases} \quad (17)$$

This solution and its evolution are shown in Fig. 2. Note that we have chosen the specific breaking time  $t_b$  in (16) so that  $a(0, t) = 1$  for  $t \leq 0$ . Any desired breaking time can be achieved by a simple time shift.

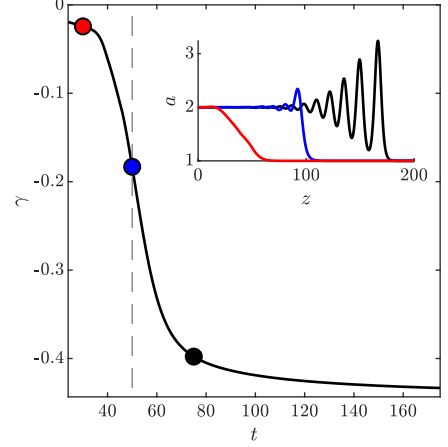


FIG. 4. Leading edge slope  $\gamma(t)$  in eq. (18) extracted from the numerical simulation depicted in Fig. 3 and the inset. The time of breaking  $t_b$  occurs at the inflection point  $\dot{\gamma}(t_b) = 0$  of the slope as a function of time (middle circle). Inset: three profiles in space corresponding to the marked points in time. The predicted breaking time is  $t_b = 50$ .

### C. Definition of Dispersive Wavebreaking Point

In order to compare the predicted versus actual dispersive wavebreaking profile, we have performed direct numerical simulations of the conduit equation (4) with the boundary condition (17) for  $z_b = 100$ ,  $t_b = 50$ , and  $a_b = 2$ . A space-time contour plot of the simulation and its comparison with the predicted step profile are shown in Fig. 3. Near the point of breaking, dispersion is no longer negligible; as a result, a perfect Riemann step is not realized in the conduit equation. Therefore, we introduce a definition of dispersive wavebreaking as follows.

By an analysis of numerical simulations of the conduit equation (4) for a variety of breaking points  $(z_b, t_b)$  and amplitudes  $a_b$ , we introduce a robust definition of the space-time location of wavebreaking from numerical simulations and experiment using the slope,  $\gamma$ , at the wave front's midpoint

$$\gamma(t) = \left. \frac{\partial a}{\partial z}(z, t) \right|_{z=z_m(t)}, \quad \text{where } z_m(t) \text{ satisfies} \quad (18)$$

$$a(z_m, t) = \frac{1}{2} \left( \max_z a(z, t) \right) + \frac{1}{2} \left( \min_z a(z, t) \right).$$

We define the breaking time for both numerical simulation and experiment as the time  $t_b$  when the slope achieves an inflection point in time:  $\dot{\gamma}(t_b) = 0$ . We then define the breaking height  $z_b$  as the location where the profile achieves its maximum amplitude:  $a(z_b, t_b) = \max_z a(z, t_b)$ . The breaking point  $(z_b, t_b)$  identified by the dashed lines in Fig. 3 corresponds to the inflection point of the slope  $\gamma(t)$  evolution shown in Fig. 4.

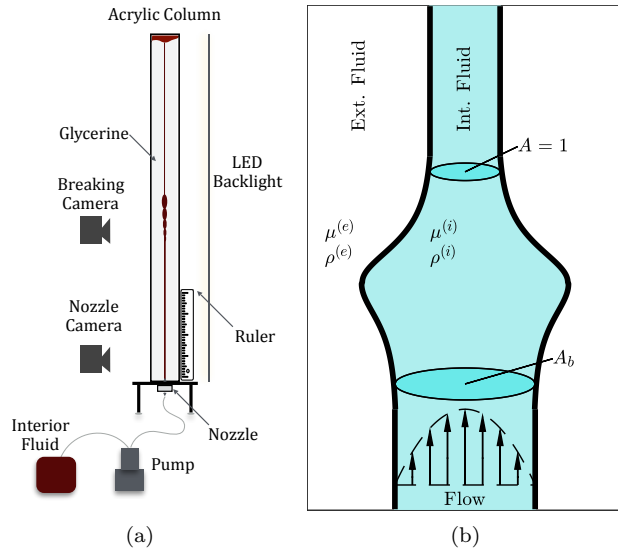


FIG. 5. (a) Schematic of the experimental setup. (b) Schematic of the conduit near  $t = t_b$ . Dispersion leads to the emergence of a nonmonotonic profile near the time of breaking.

#### D. Generalizations to Piecewise Linear Profiles

This method of neglecting the dispersive term can be used to generate a variety of initial conditions, the formulae for which are included in the appendix. In Fig. 1, we show characteristic plots based on the dispersionless approach to generate a step in Fig. 1(a), a box in Fig. 1(b), a triangle in Fig. 1(c), and an N-wave in Fig. 1(d).

There are some restrictions on the types of profiles we can generate. In order for an entire profile to be above the  $z = 0$  boundary at the time of breaking, we require the width of the profile to be less than or equal to  $z_b$ . For triangle waves and N-waves, there is an additional width-height ratio that must be satisfied in order for the diagonal portions to be fully realized. These conditions are listed in the appendix.

### III. EXPERIMENT

#### A. Setup

The experimental apparatus shown in Fig. 5(a) consists of a square acrylic column with dimensions  $4\text{ cm} \times 4\text{ cm} \times 92\text{ cm}$ ; the column is filled with glycerine a highly viscous, transparent, exterior fluid. A nozzle is installed at the base of the column to allow for the injection of the interior fluid. To eliminate surface tension effects, the interior fluid is a solution of glycerine, deionized water, and black food coloring. As a result, the interior fluid has both lower viscosity and density than the exterior fluid ( $\mu^{(i)} \ll \mu^{(e)}$ ,  $\rho^{(i)} < \rho^{(e)}$ ) and we assume mass diffusion is negligible.

Interior fluid is drawn from a separate reservoir and injected through the nozzle via a high precision computer controlled piston pump. The interior fluid rises buoyantly. By injecting at a constant rate, a vertically uniform fluid conduit is established. This uniform steady state is referred to as the background conduit, and is well-approximated as pipe (Poiseuille) flow, verified in [9]. Data acquisition is performed using high resolution cameras equipped with macro lenses at the injection nozzle and the predicted breaking height. A ruler is positioned beside the column within camera view for calibration purposes and to determine the observed breaking height.

#### B. Methods

In order to use the results from Section II, we rescale (17) from the nondimensional conduit equation (lower case variables) to physical parameters (upper case variables). Following the scaling in (3) and the Poiseuille flow relation,

$$Q = \frac{\pi g \Delta}{8\mu^{(i)}} R^4, \quad (19)$$

where  $R$  is the conduit radius, a volumetric flow rate profile  $Q(t)$  is generated for the desired wavebreaking configuration; see the appendix. The camera near the nozzle takes images before and after the initiation of the boundary volumetric flow profile, so background conduit diameters are measured. The breaking camera takes several high-resolution images before, during, and after the time of breaking. A schematic of the conduit near the height and time of breaking is shown in Fig. 5(b). After breaking occurs, the pump is reduced to the background rate  $Q_0$ , and the conduit is left to equilibrate before the next trial while fluid is extracted from the top of the fluid column.

The images from the camera are processed in MATLAB to extract the conduit edges as shown in Fig. 6(a) by taking a horizontal row of pixels and calculating the maximum and minimum derivatives for each row. As the background is white and the conduit is black, this identifies the conduit boundary. The edge data is then processed with a low-pass filter to reduce noise due to pixelation of the photograph and any impurities (such as bubbles) in the exterior fluid. The conduit diameter is then calculated as the number of pixels between the two edges.

We calibrate the ratio  $\mu^{(i)}/\Delta$  by fitting the observed diameter data and its corresponding nominal volumetric flow rate to the Poiseuille flow relation (19). We then determine the experimental breaking height  $z_b$  and time  $t_b$  using the definition in Section II C. Experimental profiles of pre-breaking, breaking, and post-breaking compared with the desired step profile are shown in Fig. 6(b).

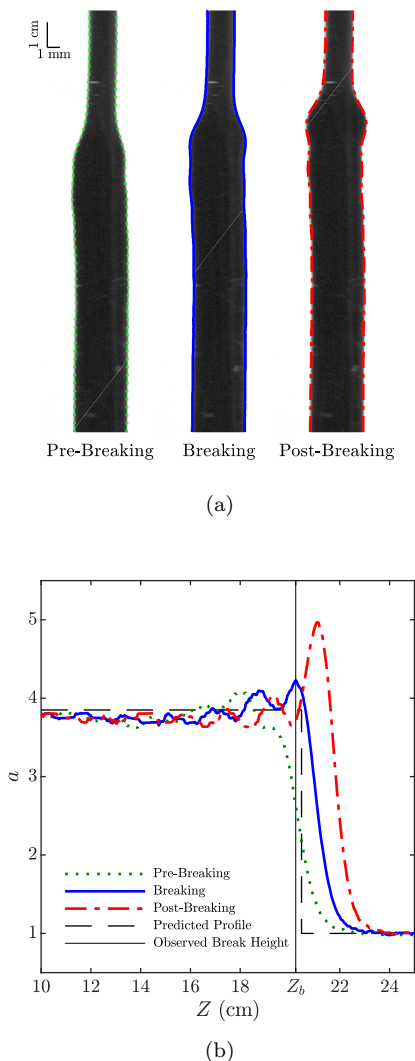


FIG. 6. (a) Processed images from a glycerine trial. Measured parameter values are  $\mu^{(i)} = 72 \pm 1\text{cP}$ ,  $\rho^{(i)} = 1.222 \pm 0.001\text{g/cm}^3$ ,  $\mu^{(e)} = 1190 \pm 20\text{cP}$ ,  $\rho^{(e)} = 1.262 \pm 0.001\text{g/cm}^3$ , and  $Q_0 = 0.25 \pm 0.01\text{ml/min}$ . The grayscale images are overlaid with the extracted conduit edges. (b) Nondimensional area plot corresponding to the images in (a). The vertical line indicates the desired step front that results from the procedure in Section III B. The dashed line indicates the expected step in a dispersionless system. Predictions were fit to the found Poiseuille flow relation (19).

### C. Results for Step Profile

Utilizing the theoretically prescribed boundary condition (A.1) that results in the step profile (5) at  $(z, t) = (z_b, t_b)$  for the solution of the dispersionless equation  $a_t + 2aa_z = 0$  with unit step initial condition, we perform numerical simulations of the full conduit equation (4) and carry out fluid experiments. A typical numerical simulation is depicted in the contour plot of Fig. 3. The wave profile steepens until dispersion becomes important, coinciding with the emergence of oscillations, which pre-

vent the formation of a discontinuity. Nevertheless, using the method described in the previous section to extract  $(z_b, t_b)$  from the simulations, the observed breaking locations and times are within 3.75% and 1.35% relative error, respectively of their predicted values across a range of step ratios and breaking heights as depicted by the triangles and dashed lines in Fig. 7.

For the experiment, thirteen trials were taken over the course of four hours. The main results of this experiment are also shown in Fig. 7. The predicted breaking heights and times ( $z_{b,in}$  and  $t_{b,in}$ ) (denoted with dashed lines) are very close to the experimentally observed values ( $z_{b,out}$  and  $t_{b,out}$ ) (denoted by squares). Figure 7 includes the theoretical prediction, numerical simulations, and experiment for the breaking height (a) and the breaking time (b). All experiments were under 5% relative error in breaking height  $z_b$  and 2.5% relative error in breaking time  $t_b$ . Therefore, a high degree of wavebreaking control is achieved by our approach. Furthermore, the prediction's accuracy appears to be independent of the breaking amplitude  $A_b$ , which is consistent with the dimensional analysis requirement (9) that is independent of wave amplitude.

These observations extend previous experimental comparisons of theoretical predictions for the conduit equation involving solitons [2, 6–8] and dispersive shock waves [9, 10]—i.e., nonlinear, *dispersive* waves—into the non-dispersive, nonlinear regime. It is noteworthy that theoretical predictions derived from the relatively simple inviscid Burgers model,  $a_t + 2aa_z = 0$ , agree so well with numerical simulations and experiment across a range of parameter values.

### D. Results for Triangle, N, and Box Profiles

Experiments were also performed for other wavebreaking profiles. Experiments on boundary conditions for generating triangle waves (A.3) and N-waves (A.5) showed good fidelity to the expected shapes, as shown in Fig. 8. Moreover, we obtain quantitative agreement between the predicted characteristics (recall Fig. 1(c,d)) and the observed curves of equi-area pre-breaking as shown by the dashed lines overlaid on the cross-sectional area contour plot. For the figure, we fit  $z_b$  and  $t_b$  to those found experimentally, then generated the predicted characteristics (contours) based on these values. We find this fitting method is equivalent to fitting  $\mu^{(i)}/\Delta$  to the data, similar to what was done for the step profile.

As an application of our approach to generating desired wave profiles at breaking, we show an experimental and numerical realization of solitary wave fission [21] from the long-time dynamics of a box profile in Figs. 9(a) and 9(b), respectively. The boundary time-series for the box profile, eq. (A.2), results in an approximately rectangular-shaped area profile with a specified width and height. The long-time evolution of this profile re-

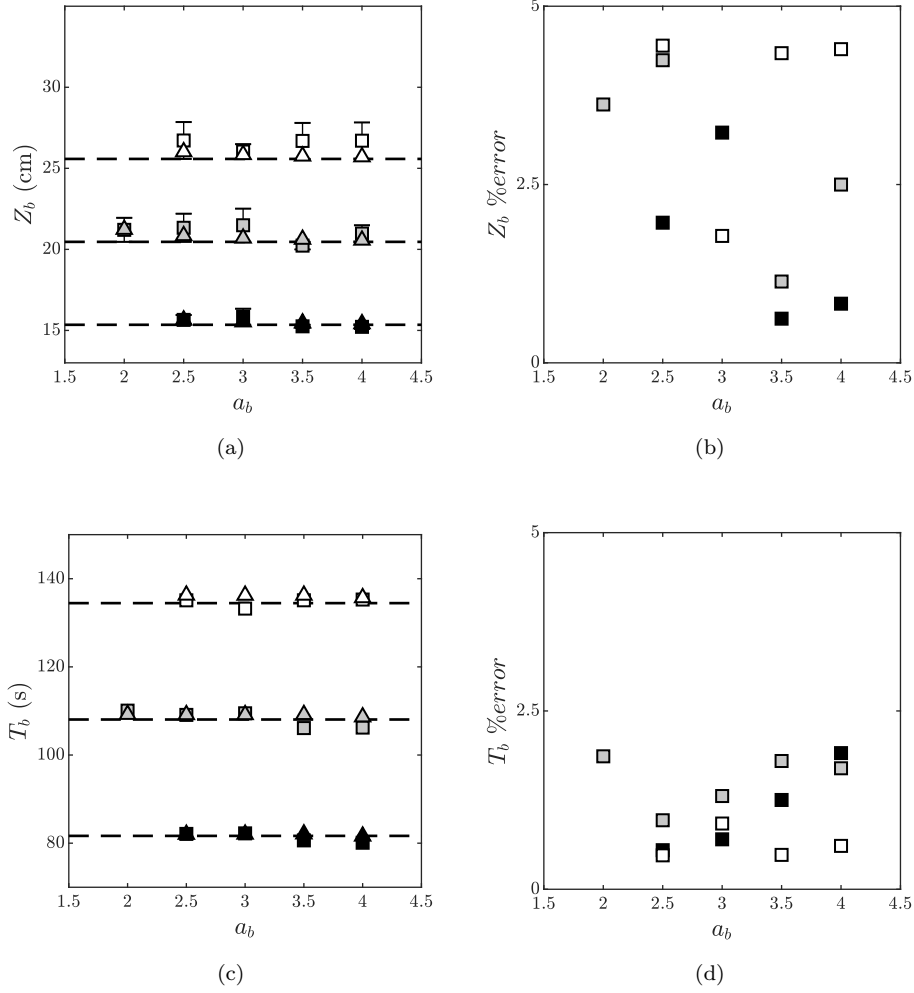


FIG. 7. Comparison of dispersionless (long-wave) theory (dashed lines), full conduit equation numerics (triangles) and glycerine experiments (squares) for the step wavebreaking configuration. (a) Breaking height results and (b) relative error for experiments as a function of jump ratio  $a_b$ , with the same fluid parameters as those in Fig. 6. (c) Breaking time results and (d) relative error for those same experiments. Note the breaking time error bars are smaller than the symbols used. The black squares correspond to an expected  $z_b = 15.3$  cm, the gray to  $z_b = 20.5$  cm, and the white to  $z_b = 25.6$  cm.

sults in a train of solitary waves. The numerical simulation in Fig. 9(b), generated by the same boundary control procedure, exhibits excellent agreement with the experiment in Fig. 9(a) for the experimental volumetric flow rate  $Q_0 = 0.2 \text{ mL min}^{-1}$  if we introduce the fitted values  $\mu^{(i)}/\Delta = 724 \text{ cm}^2 \text{ min}^{-1}$  and  $\mu^{(i)}/\mu^{(e)} = 0.05$  (measured values  $\mu^{(i)}/\Delta = 1087 \text{ cm}^2 \text{ min}^{-1}$  and  $\mu^{(i)}/\mu^{(e)} = 0.02$ ). Future work aims to explore the post-breaking dynamics of this and other dispersive hydrodynamic problems by leveraging the boundary control method introduced here.

#### IV. CONCLUSION

While previous experimental and theoretical work on the conduit equation and its corresponding viscous two-

fluid system have primarily focused on dispersive hydrodynamics *post-breaking*, i.e., when nonlinearity and dispersion are important, this work considers the simpler case of very long waves where nonlinearity dominates the flow. A simple long-wave hyperbolic model (the inviscid Burgers equation) is used to theoretically control nonlinear wave propagation at the interface of a viscous fluid conduit prior to wavebreaking. The pre-breaking validity of the hyperbolic model enables the precise creation of desired wavebreaking profiles in the interior of the dispersive hydrodynamic domain with only boundary control. Characteristics are propagated backward in time from a desired wave profile until they reach the boundary. So long as the backward characteristics do not overlap, it is possible to obtain a boundary condition whose forward propagation approximately results in the desired wave-



breaking profile.

In order to compare this dispersionless theory with the “dispersionfull” conduit equation and experiment, we define wavebreaking by an inflection point criterion for the wavefront’s slope. This definition provides a bridge between the long-wave, pre-breaking dynamics and the short-wave oscillations that emerge post-breaking. Most importantly, we obtain quantitative agreement between theory, numerical simulation, and experiment with this wavebreaking definition. For a step profile, the observed breaking heights and times are within 5% and 2.5%, respectively, of their expected values. For more complex

profiles—the triangle and N-wave configurations—we obtain good characteristic control observed in measured space-time contour plots. One example of post-breaking dispersive hydrodynamics is highlighted where a large number of solitary waves emerges from a large box profile. Numerical simulation and experiment utilizing the same box profile boundary condition result in striking agreement and motivate further analysis of the soliton fission problem in the context of the viscous fluid conduit system. The relatively simple characteristic method proposed here holds promise for other dispersive hydrodynamic media.

- 
- [1] G. A. El and M. A. Hoefer, “Dispersive shock waves and modulation theory,” *Physica D: Nonlinear Phenomena* **333**, 11 – 65 (2016).
  - [2] P. Olson and U. Christensen, “Solitary wave propagation in a fluid conduit within a viscous matrix,” *Journal of Geophysical Research: Solid Earth* **91**, 6367 (1986).
  - [3] N. K. Lowman and M. A. Hoefer, “Dispersive hydrodynamics in viscous fluid conduits,” *Phys. Rev. E* **88**, 023016 (2013).
  - [4] J. A. Whitehead and K. R. Helfrich, “Wave transport of deep mantle material,” *Nature* **336**, 59 (1988).
  - [5] M. D. Maiden and M. A. Hoefer, “Modulations of viscous fluid conduit periodic waves,” *Proc. Royal Soc. Lond A: Mathematical, Physical and Engineering Sciences* **472** (2016), 10.1098/rspa.2016.0533.
  - [6] D. R. Scott, D. J. Stevenson, and J. A. Whitehead, “Observations of solitary waves in a viscously deformable pipe,” *Nature* **319**, 759–761 (1986).
  - [7] K. R. Helfrich and J. A. Whitehead, “Solitary waves on conduits of buoyant fluid in a more viscous fluid,” *Geophysical & Astrophysical Fluid Dynamics* **51**, 35–52 (1990).
  - [8] N. K. Lowman, M. A. Hoefer, and G. A. El, “Interactions of large amplitude solitary waves in viscous fluid conduits,” *Journal of Fluid Mechanics* (2013).
  - [9] M. D. Maiden, N. K. Lowman, D. V. Anderson, M. E. Schubert, and M. A. Hoefer, “Observation of dispersive shock waves, solitons, and their interactions in viscous fluid conduits,” *Phys. Rev. Lett.* **116**, 174501 (2016).
  - [10] M. D. Maiden, D. V. Anderson, N. A. Franco, G. A. El, and M. A. Hoefer, “Solitonic dispersive hydrodynamics: Theory and observation,” *Phys. Rev. Lett.* **120**, 144101 (2018).
  - [11] D. H. Peregrine, “Calculations of the development of an undular bore,” *J. Fluid Mech.* **25**, 321–330 (1966).
  - [12] A. V. Gurevich and L. P. Pitaevskii, “Nonstationary structure of a collisionless shock wave,” *JETP* **38**, 291–297 (1974), translation from Russian of A. V. Gurevich and L. P. Pitaevskii, *Zh. Eksp. Teor. Fiz.* 65, 590–604 (August 1973).
  - [13] G. B. Whitham, *Linear and nonlinear waves* (Wiley-Interscience [John Wiley & Sons], 1974) pure and Applied Mathematics.
  - [14] R. Courant and K. O. Friedrichs, *Supersonic Flow and Shock Waves* (Springer-Verlag, 1948).
  - [15] S. Trillo, M. Klein, G. F. Clauss, and M. Onorato, “Observation of dispersive shock waves developing from initial depressions in shallow water,” *Physica D: Nonlinear Phenomena* **333**, 276 – 284 (2016), dispersive Hydrodynamics.
  - [16] Gang Xu, Matteo Conforti, Alexandre Kudlinski, Arnaud Mussot, and Stefano Trillo, “Dispersive dam-break flow of a photon fluid,” *Phys. Rev. Lett.* **118**, 254101 (2017).
  - [17] P. A. Praveen Janantha, Patrick Sprenger, Mark A. Hoefer, and Mingzhong Wu, “Observation of self-cavitating envelope dispersive shock waves in yttrium iron garnet thin films,” *Phys. Rev. Lett.* **119**, 024101 (2017).
  - [18] C. Chong, M. A. Porter, P. G. Kevrekidis, and C. Daraio, “Nonlinear coherent structures in granular crystals,” *Journal of Physics: Condensed Matter* **29**, 413003 (2017).
  - [19] Benjamin Wetzel, Domenico Bongiovanni, Michael Kues, Yi Hu, Zhigang Chen, Stefano Trillo, John M. Dudley, Stefano Wabnitz, and Roberto Morandotti, “Experimental generation of riemann waves in optics: A route to shock wave control,” *Phys. Rev. Lett.* **117**, 073902 (2016).
  - [20] G. B. Whitham, “Non-linear dispersive waves,” *Proc. Royal Soc. Lond A: Mathematical, Physical and Engineering Sciences* **283**, 238 (1965).
  - [21] S. Trillo, G. Deng, G. Biondini, M. Klein, G. F. Clauss, A. Chabchoub, and M. Onorato, “Experimental Observation and Theoretical Description of Multisoliton Fission in Shallow Water,” **117**, 144102.
  - [22] N. Ghofraniha, L. Santamaria Amato, V. Folli, S. Trillo, E. DelRe, and C. Conti, “Measurement of scaling laws for shock waves in thermal nonlocal media,” **37**, 2325–2327.
  - [23] J. A. Whitehead and D. S. Luther, “Dynamics of Laboratory Diapir and Plume Models,” *Journal of Geophysical Research* **80**, 705–717 (1975).

#### Appendix: Boundary Conditions for Wavebreaking Profiles

All following profiles have a breaking time  $t_b$  based on the breaking height  $z_b$  of  $t_b = z_b/2$ .

The boundary condition  $a(0, t)$  resulting in an approx-

imate step profile for (4) (see Fig. 1a)

$$a(0, t) = \begin{cases} 1 & : & t \leq 0 \\ (1 - 2t/z_b)^{-1} & : & 0 < t < \frac{(a_b-1)}{2a_b} z_b \\ a_b & : & t \geq \frac{(a_b-1)}{2a_b} z_b \end{cases} \quad (\text{A.1})$$

For a box, this profile is cut off at the time of breaking  $t_b = z_b/2$  (see Fig. 1b)

$$a(0, t) = \begin{cases} 1 & : & t \leq 0 \\ (1 - 2t/z_b)^{-1} & : & 0 < t < \frac{(a_b-1)}{2a_b} z_b \\ a_b & : & \frac{(a_b-1)}{2a_b} z_b \leq t < \frac{z_b}{2} \\ 1 & : & t \geq \frac{z_b}{2} \end{cases} \quad (\text{A.2})$$

For a right triangle with height  $a_b$ , width  $w$ , and hypotenuse slope  $m = \frac{a_b-1}{w}$ , once the maximum desired height is reached, we begin decreasing the flow rate in a way consistent with Eq.(14) (see Fig. 1c)

$$a(0, t) = \begin{cases} 1 & : & t < 0 \\ (1 - 2t/z_b)^{-1} & : & 0 \leq t < \frac{(a_b-1)}{2a_b} z_b \\ \frac{-mz_b+a_b}{1-mz_b+2mt} & : & \frac{(a_b-1)}{2a_b} z_b \leq t < \frac{w}{2} \\ 1 & : & t \geq \frac{w}{2} \end{cases} \quad (\text{A.3})$$

The width-height restrictions on the triangle wave are based on having the triangle fully in the conduit at the time of breaking as well as the non-breaking condition  $a'_0(z) < 1/2t_b$

$$1 \leq \frac{z_b}{w} \leq \frac{1}{a_b - 1} \quad (\text{A.4})$$

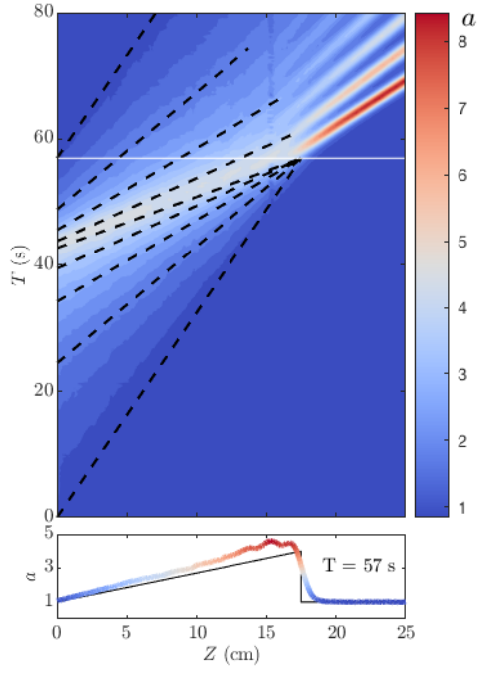
For an N-wave with maximum height  $a_{max}$ , minimum height  $a_{min}$ , width  $w$ , and slope  $m = \frac{a_{max}-a_{min}}{w}$ , we generate a triangle wave whose final area dips below the mean flow rate down to  $a_{min}$  before returning to the mean flow (see Fig. 1d)

$$a(0, t) = \begin{cases} 1 & : & t < 0 \\ (1 - 2t/z_b)^{-1} & : & 0 \leq t < \frac{(a_{max}-1)}{2a_{max}} z_b \\ \frac{-mz_b+a_{max}}{1-mz_b+2mt} & : & \frac{(a_{max}-1)}{2a_{max}} z_b \leq t < \frac{w-(1-a_{min})z_b}{2a_{min}} \\ \frac{z_b-w}{z_b-2t} & : & \frac{w-(1-a_{min})z_b}{2a_{min}} \leq t < \frac{w}{2} \\ 1 & : & t \geq \frac{w}{2} \end{cases} \quad (\text{A.5})$$

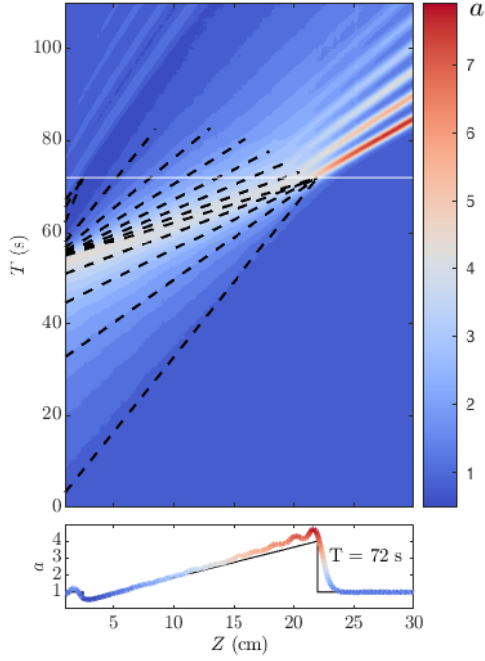
The N-wave width-height restrictions are also based on having the wave fully in the conduit at the time of breaking and the non-breaking condition  $a'_0(z) < 1/2t_b$

$$1 \leq \frac{z_b}{w} \leq \frac{1}{a_{max} - a_{min}} \quad (\text{A.6})$$

Note when  $w \rightarrow \infty$  and  $a_{min} = a_{max} = a_b$ , we arrive at Eq. (17).



(a)



(b)

FIG. 8. Experimental data for triangle wave (top) and N-wave (bottom) boundary conditions. Overlay lines: fitted characteristic data for triangle (a) and N-wave (b) profiles.

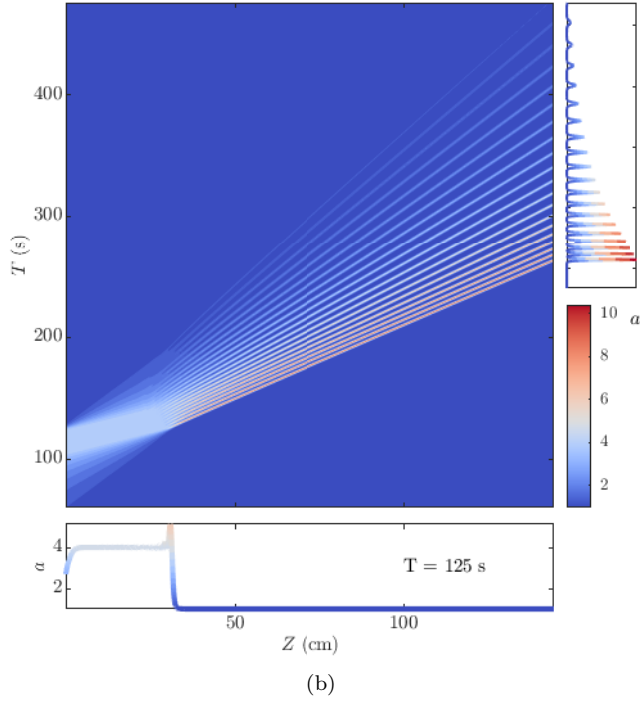
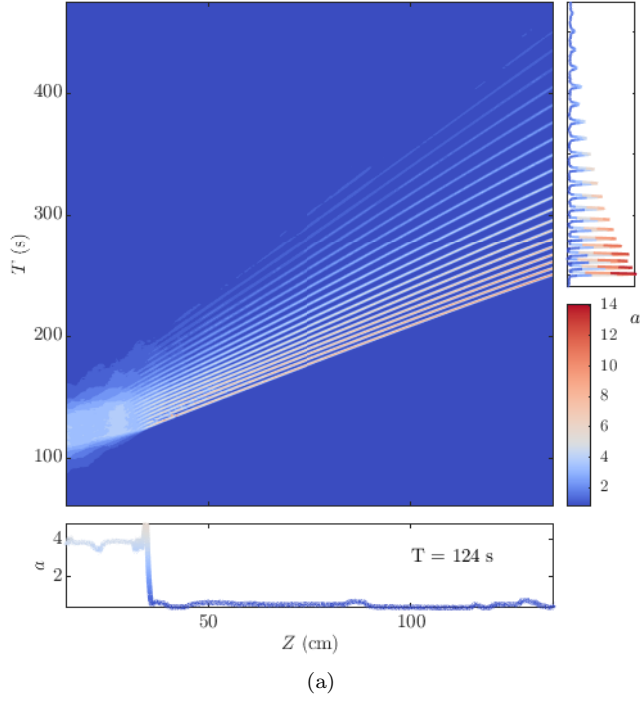


FIG. 9. Evolution of the box profile resulting in a train of solitary waves. (a) Experiment. (b) Conduit equation numerical simulation. Both experiment and numerical simulation utilized the boundary condition (A.2).